Supporting Information

Rapid synthesis of CuZn-MOF via controlled electrodeposition: Manifest enhanced overall electrocatalytic water splitting

Aashi, Srinivasan Alagar, Krishankant, Ashish Gaur, Chandan Bera and Vivek Bagchi*

Energy and Environment Research Lab, Institute of Nano Science and Technology, Sector -81, Knowledge City, Sahibzada Ajit singh Nagar, Punjab, Pin-140 306, India.

*Corresponding Author

Dr. Vivek Bagchi

Email: vivekbagchi@gmail.com, bagchiv@inst.ac.in

Table of Contents

S1. Experimental Section

S1.1 Electrochemical Deposition of CuZn-250

CuZn-250 was electrochemically deposited utilizing a two-electrode setup with a working electrode of 1 cm x 1.5 cm NF and a counter electrode of graphitic rod. The electrolyte for electrochemical deposition (ECD) was made by dissolving 45 mM of $Cu(NO_3)_2.4H_2O$, 5 mM of $Zn(NO_3)_2.4H_2O$, in 30 ml of DMF. Thereafter, at room temperature (25 °C), ECD was performed at a constant potential of -1.5V for 250 s. After deposition, the electrodes were washed with DI water and ethanol, then dried at 70 °C (as denoted CuZn-250.

S1.2 Hydrothermal synthesis of CuZn-BTC

In typical synthesis of CuZn-BTC by hydrothermal method, dissolved the 45 mM of $Cu(NO_3)_2.4H_2O$, 5 mM of $Zn(NO_3)_2.4H_2O$, 0.1 M of BTC in 30 ml of DMF and stirred for 30 minutes. Then reaction mixture was transferred into 50 ml autoclave containing a washed NF and heated the hydrothermal for 120˚C for 12 h. After cool down to room temperature NF was washed with DI water and ethanol, and dried in an oven at 60 ˚C.

S2. Material Characterization Techniques

To determine the crystallinity of the catalyst, powder X-ray diffraction was performed in the range of 5-40° using Bruker Eco D8 advance diffractometer (Cu Kα, λ= 1.54056). The chemical states of the catalyst were determined by employing X-ray photoelectron

spectroscopy (XPS) using ESCA LAB 250 XI with a Mg Kα non-monochromate X-ray beam with a photon energy of 1253.6 eV. The surface morphology was examined by field emission scanning electron microscopy (FE-SEM) with an Apreo 2 SEM Thermo Fisher. High resolution transmission electron microscopy (HR-TEM) was carried out using JEOL 2100 at 200kV to determine the microstructure of the crystal.

S3. Electrochemical measurement of OER, HER and overall water splitting

All electrochemical studies for OER and HER were analyzed using a three-electrode system in 1M KOH (pH=13.8) electrolyte at room temperature. Ag/AgCl, graphitic rod and all synthesis electrodes were used as reference, counter and working electrode. RuO_2 and Pt/C also prepared on NF for comparison. Pt/C prepared by dispersing 5.0 mg of commercially available Pt/C in a solution containing 495 µL of ethanol and 5 µL of Nafion sol of 5 wt %, and then drop-casting this onto NF and vacuum drying it overnight. Similar procedure followed for synthesis of RuO_2 on NF. All the electrochemical data are converted into reversible hydrogen electrode (RHE) using the formula (S1):

$$E_{RHE} = E_{Ag/Agcl} + 0.197\,V + 0.059 \times pH$$

Using the following equation (S2):

$$\eta = b\,log(J) + a$$

Tafel slope was calculated by plotting the overpotential (η) versus log (J), where η represents the overpotential, b is the Tafel slope, and J is the current density. To estimate the double-layer capacitance (C_{dl}), cyclic Voltammogram (CV) was performed in non-

faradaic region (0.09-0.19 V vs RHE for OER and -0.03 to -0.04 V vs RHE for HER) at different scan rate (50, 100, 150, 200, and 250 mV s^{-1}) as shown in Fig. S6. Then to determine the electrochemical active surface area (ESCA) using the formula (S3):

$$ECSA = \frac{C_{dl}}{C_s}$$

where C_{dl} is the double-layer capacitance and C_s is the material specific capacitance (C_s is 0.04 mF cm^{-2} for NF).[1] The turnover frequency (TOF) was estimated using the following formula (S4):

$$TOF = \frac{JS}{4mf}$$

where J is the current density, S is the geometric area, m is the number of active sites of the catalyst, and F is the Faraday constant (95,485 C mol^{-1}). To check the stability of CuZn-BTC-250 in 1M KOH solution, chronoamperometry technique was employed at 10 mA cm^{-2}. Thereafter, Faradaic efficiency was also computed using the water gas displacement method.[2]

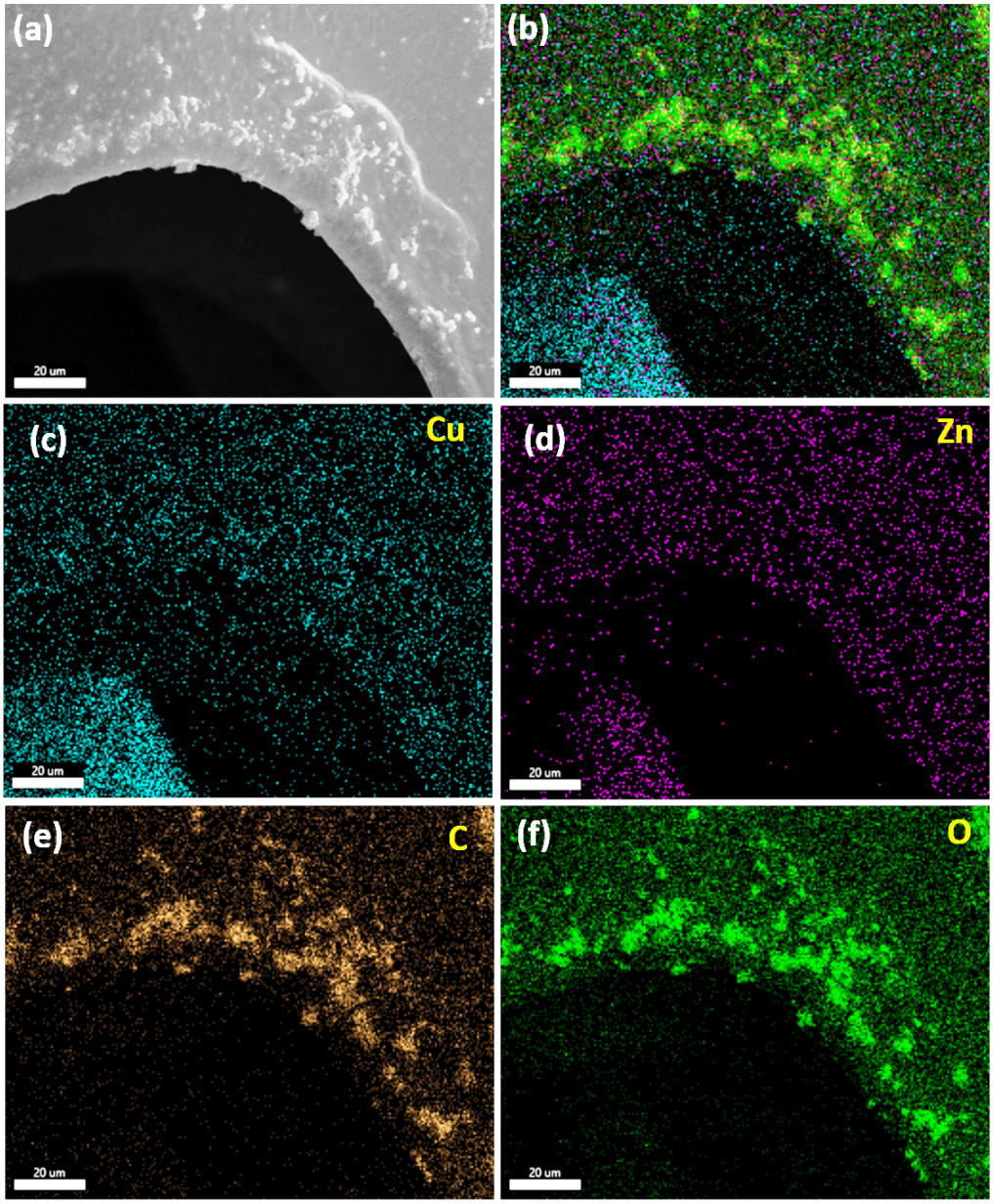

Fig. S1 FE-SEM images of CuZn-BTC-250 on NF. (a) FE-SEM image, (b) Cu, Zn, C and O elemental distribution image, (c-f) individual elements mapping of Cu, Zn, C and O elements.

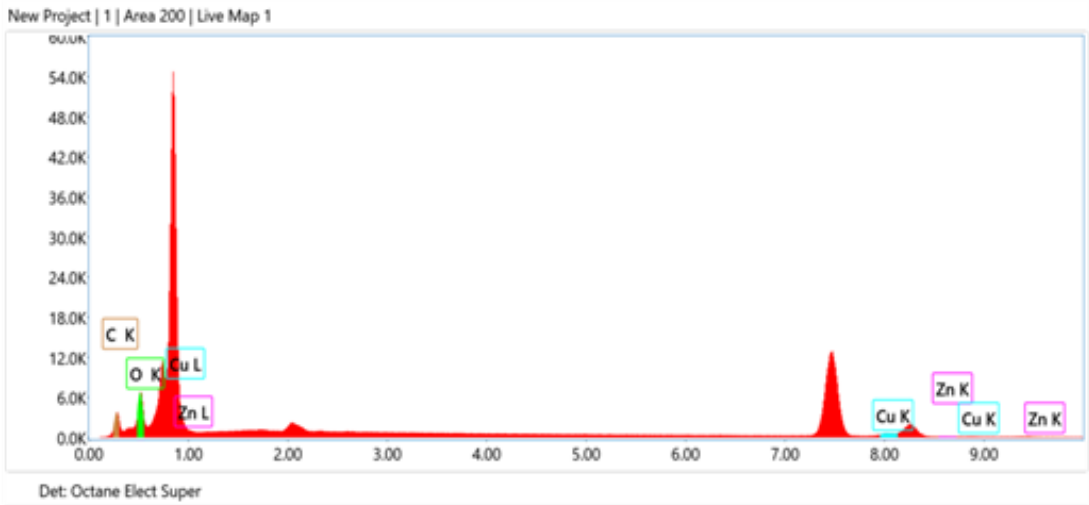

Element	Weight %	Atomic %	Net Int.	R	A	F	Error %
C K	34.6	62.3	267.1	10.9	0.8607	0.1329	1.0000
O K	15.4	20.8	456.5	9.9	0.8750	0.2042	1.0000
Cu K	44.7	15.2	404.2	4.6	0.9710	0.9945	1.0519
Zn K	5.3	1.8	35.0	12.8	0.9759	0.9935	1.0547

Fig. S2 FESEM elemental analysis of the CuZn-BTC-250.

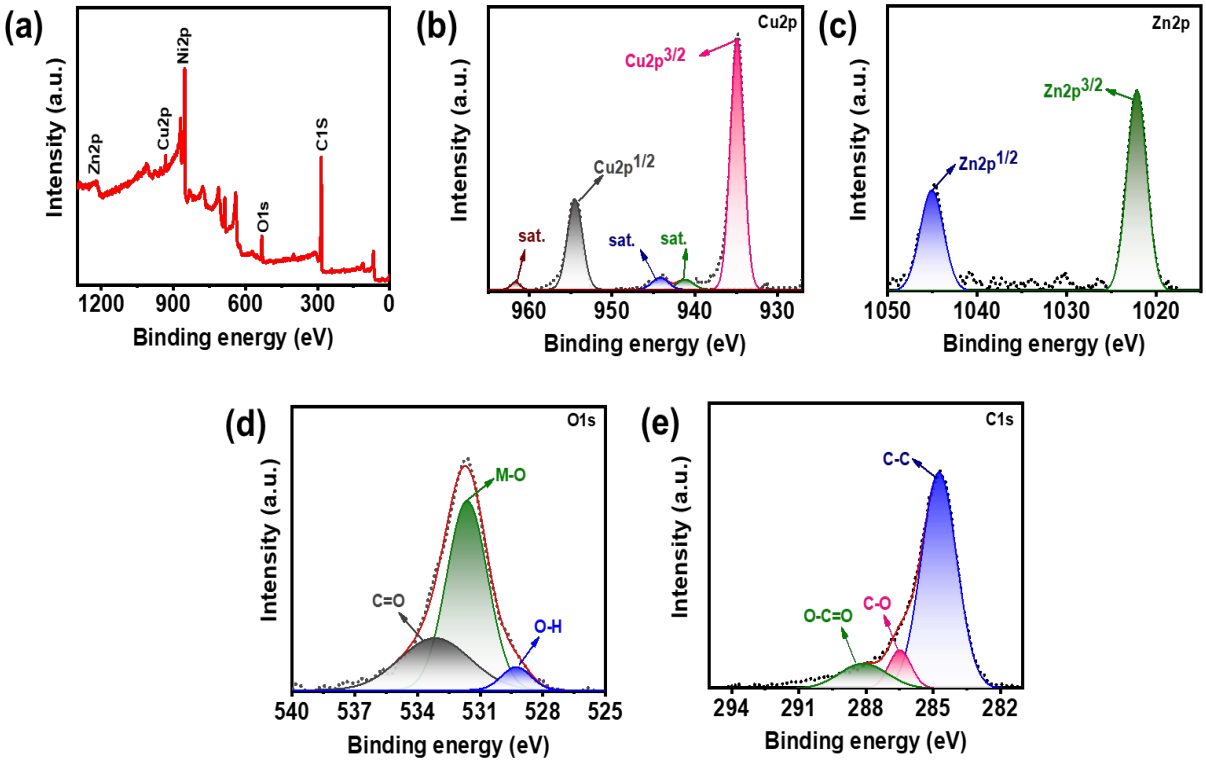

Fig. S3 (a) XPS survey spectra of CuZn-BTC-250, high resolution spectra of (b) Cu 2p, (c) Zn 2p, (d) O 1s, (e) C 1s.

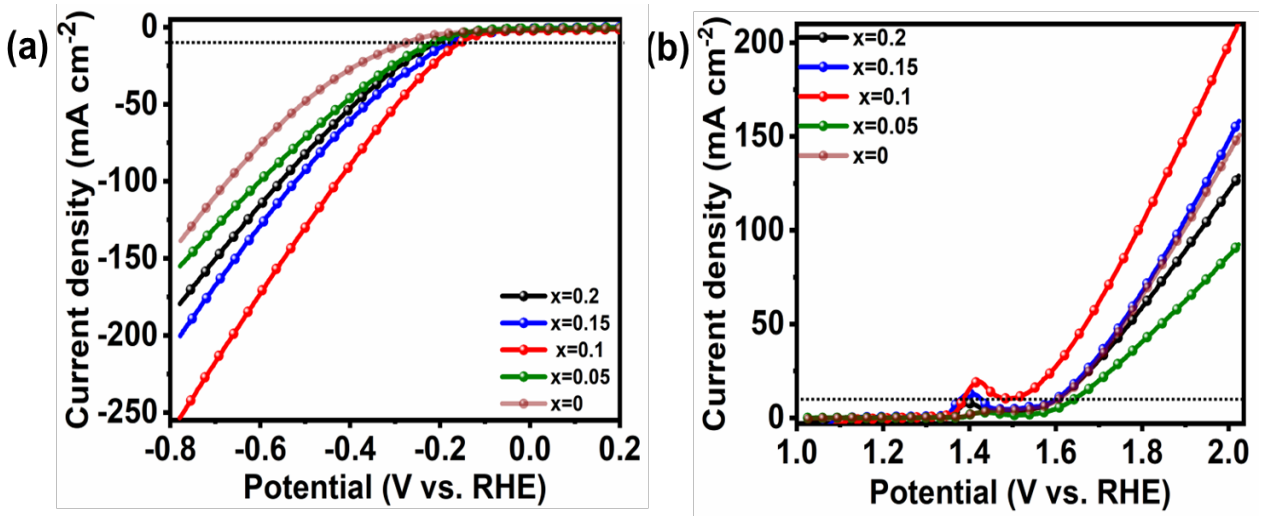

Fig. S4 LSV curve for (a) HER, and (b) OER of $Cu_{1-x}Zn_x$-BTC at different ratio, when x=0.2, 0.15, 0.1, 0.05, .and 0.

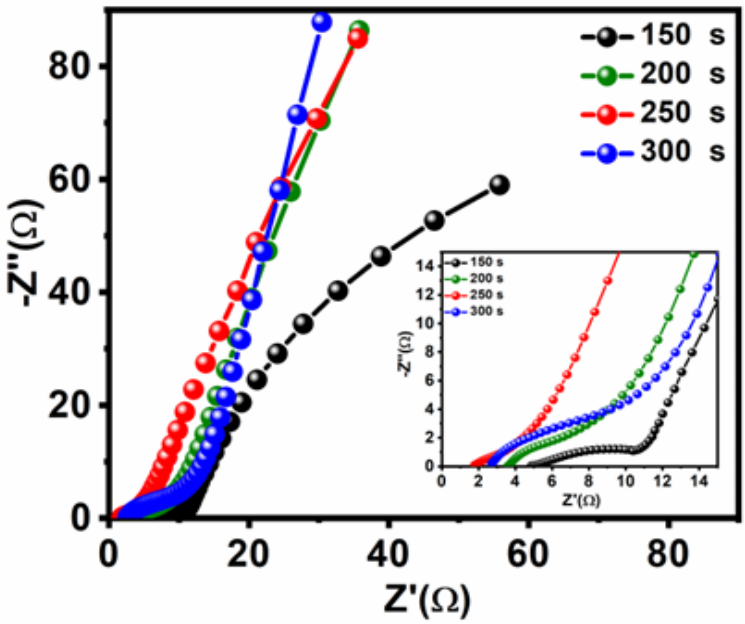

Fig. S5 Impedance of CuZn-BTC at different deposition time (15, 200, 250 and 300 s)

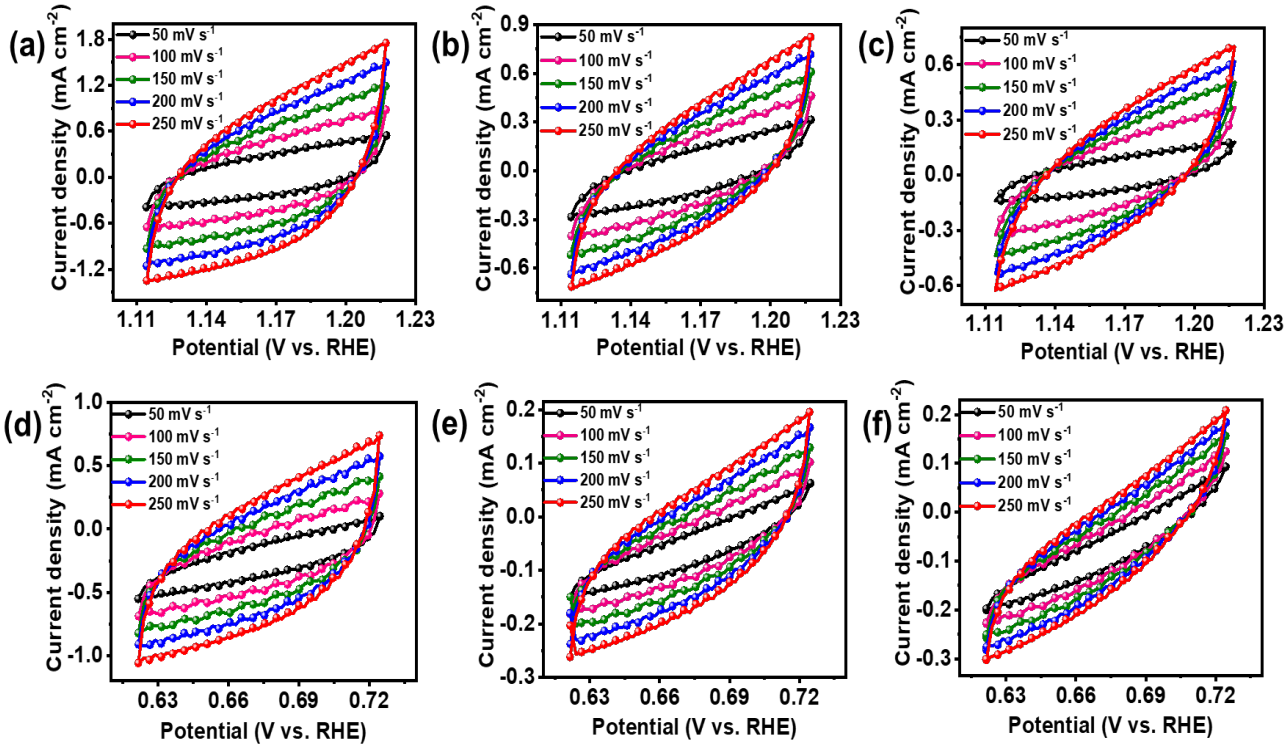

Fig. S6 CV curve of (a) CuZn-BTC-250, (b) Cu-BTC-250, (c) Zn-BTC-250 for OER, and CV curve of (d) CuZn-BTC-250, (e) Cu-BTC-250, (f) Zn-BTC-250 for HER, at different scan rate.

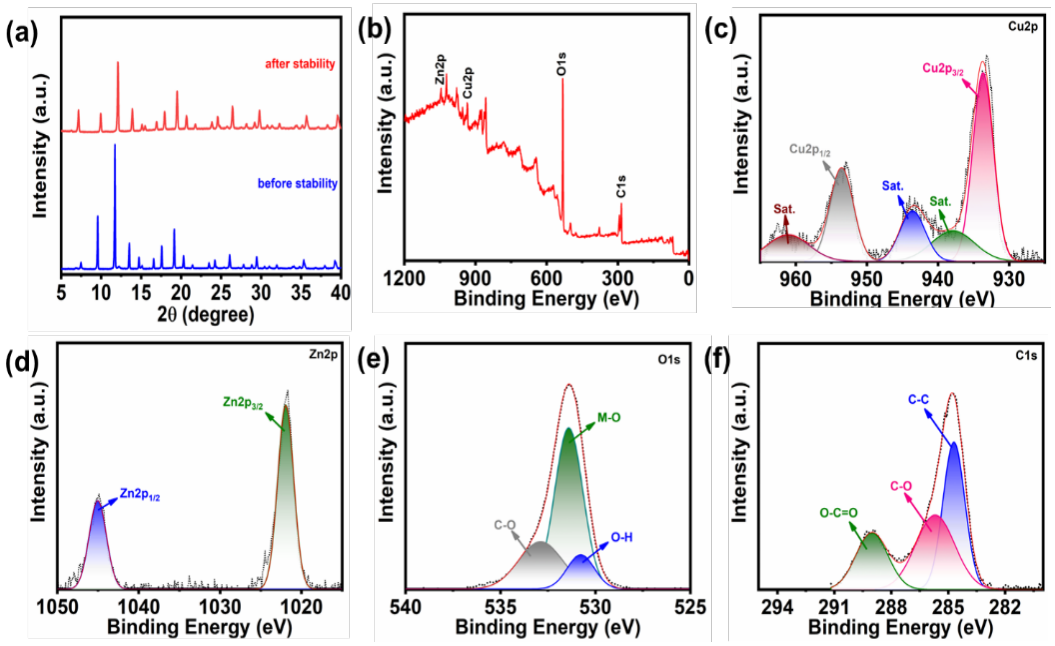

Fig S7 XRD pattern of CuZn-BTC-250 before and after stability, (b) survey spectra, high resolution spectra of (c) Cu2p, (d) Zn2p, (e) O1s, (f) C1s.

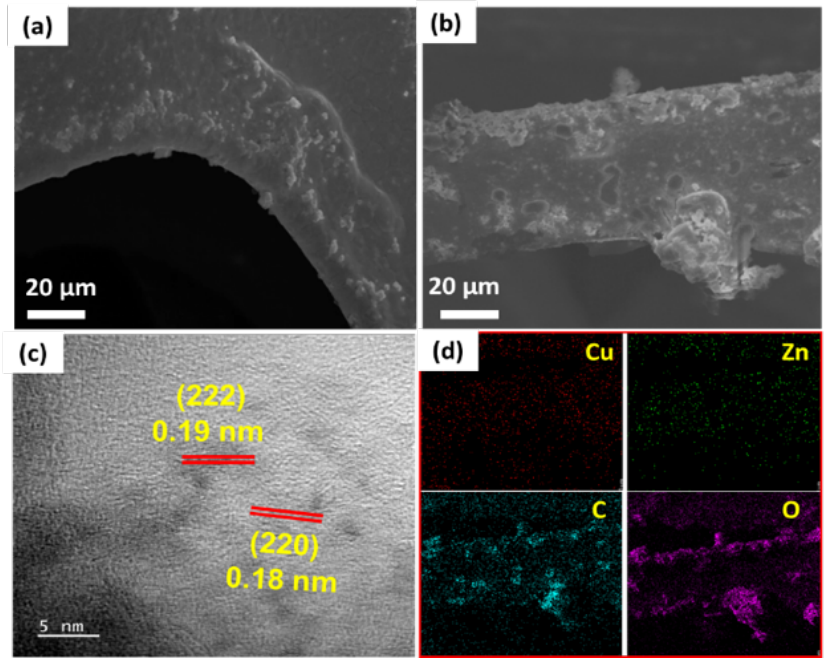

Fig. S8 FESEM image of CuZn-BTC-250 (a) before, (b) after stability, (c) HRTEM image, (d) FESEM elemental mapping of Cu, Zn, C and O of CuZn-BTC-250 after stability.

Table S1. Comparison of electrocatalytic activity CuZn-BTC-250 with recently developed MOF-based electrodes towards OER.

Electrodes	**OER**			**References**
	$E_{J= 10\ mA\ cm^{-2}}$	Tafel slope	Stability	
CuZn-BTC-250	253 mV	74 mV dec^{-1}	50 h	This work
CoBDC FcCA	280 mV	53 mV dec^{-1}	10 h	[3]
$Ti_3C_2T_x$-CoBDC	410 mV	48.2 mV dec^{-1}	3 h	[4]
CoNi-MOF	318 mV	48 mV dec^{-1}	48 h	[5]
CoCd-MOF	313 mV	110 mV dec^{-1}	5 h	[6]
Ni-MOF@Fe-MOF	265 mV	82 mV dec^{-1}	-	[7]
$CoCl_2$@Th-BPYDC	388 mV	94 mV dec^{-1}	-	[8]
FePc@Ni-MOF	334 mV	72.1 mV dec^{-1}	10 h	[9]
$A_{2.7}$B-MOF-$FeCo_{1.6}$	288 mV	39 mV dec^{-1}	11 h	[10]
Co_2-MOF@Nafion electrode	670 mV	105 mV dec^{-1}	500 Cycles	[11]
Macro-TpBpy-Co	380 mV	89 mV dec^{-1}	60 h	[12]

Table S2. Comparison of electrocatalytic activity of CuZn-BTC-250 with recently developed MOF-based electrodes towards HER.

Electrodes	**HER**			**References**
	$E_{J= 10\ mA\ cm^{-2}}$	Tafel slope	Stability	
CuZn-BTC-250	152 mV	134.3 mV dec^{-1}	50 h	This work
NiS_2 HMSs	219 mV	157 mV dec^{-1}	20 h	[13]
CoTHT-mof	143 mV	70.6 mV dec^{-1}	24 h	[14]
Fe_2Zn-MOF	221 mV	174 mV dec^{-1}	24 h	[15]
$Cu_{0.3}Co_{2.7}P$/NC	220 mV	120 mV dec^{-1}	50 h	[16]
NENU-500	237 mV	96 mV dec^{-1}	2000 cv cycles	[17]
MOF NiS@NU-1000	238 mV	111 mV dec^{-1}	2 h	[18]
NiCoFeB	350 mV	98 mV dec^{-1}	10 h	[19]
Mo_2C/UiO-66	174 mV	147 mV dec^{-1}	24 h	[20]
Y–S Ni–Co-Se/CFP	252 mV	72 mV dec^{-1}	18 h	[21]
CuO@UiO-66	220 mV	164 mV dec^{-1}	10 min	[22]

Table S3. Comparison of electrocatalytic activity of CuZn-BTC-250 with recently developed MOF-based electrodes towards overall water splitting.

Sample	**Overall water splitting**		**Reference**
Materail	E_J / mV (J = 10 mA cm^{-2})	Stability	
CuZn-BTC	1.63 V	120 h	This work
NFN-MOF/NF	1.56 V	30 h	[23]
FeCoMnNi-MOF-74/NF	1.62 V	30 h	[24]
PNC/Co	1.64 V	-	[25]
Co,Fe-MOF-74/Co/CC	1.65 V	70 h	[26]
Mn-MOF/NF	1.68 V	4 h	[27]
Fe-ZIF-67 NFs	1.68 V	12 h	[28]
$Cu_{0.3}Co_{2.7}P$/NC	1.74 V	50 h	[15]
NiCoFeB	1.81 V	20 h	[19]

S4. Computational details

Density functional theory (DFT) calculations was performed using the Vienna Ab initio Simulation Package (VASP) to further estimate the active site of the catalyst, Gibb's free energy, and mechanism of the CuZn-BTC catalyst[29]. In DFT calculations, to avoid the periodic imaging interaction a 10 Å vacuum was established in Z- direction and a 1 × 1 × 1 supercell of 38 atoms with a=15 Å, b= 13 Å, c= 22 Å was created. A K-mesh with a 7 × 7 × 1 γ-center has been selected, with the cutoff energy set at 520 eV. For the structural optimization, the energy convergence was set at 10^{-4} eV, and the forces converged within 0.01 eV $Å^{-1}$.

The mechanism of OER in alkaline medium involves four steps as described below:

$$M^* + OH^- \rightarrow M - OH^* + e^- \quad \text{(i)}$$

$$M - OH^* + OH^- \rightarrow M - O^* + H_2O + e^- \quad \text{(ii)}$$

$$M - O^* + OH^- \rightarrow M - OOH^* + e^- \quad \text{(iii)}$$

$$M - OOH^* + OH^- \rightarrow -M^* + O_2 + H_2O + e^- \quad \text{(iv)}$$

Where, O, OH, OOH is the intermediate adsorbed on the active sites, M is the metal and * indicates the active site of the metal.

Using the following equations, adsorption energies of each intermediate was evaluated to determine the active site:

$$\Delta E_{OH^*} = E_{OH^*} - E^* - E_{H_2O} + \frac{1}{2}E_{H_2}$$

$$\Delta E_{O^*} = E_{O^*} - E^* - E_{H_2O} + E_{H_2}$$

$$\Delta E_{OOH^*} = E_{OOH^*} - E^* - 2E_{H_2O} + \frac{3}{2}E_{H_2}$$

To determine the adsorption Gibbs free energy of adsorbents (ΔG_{ads}) for OER using the following formula, which is an important indicator of whether the process might occur spontaneously [30].

$$\Delta G_{ads} = \Delta E_{ads} + \Delta E_{ZPE} - T\Delta S + \Delta G_u + \Delta G_{pH}$$

Where, ΔE_{ZPE}, ΔS and T are the difference in zero-point energy, difference in entropy and temperature of the system, respectively and the terms ΔE_{ZPE} and $T\Delta S$ are considered to be zero to simplify the calculation. ΔG_u represents the applied electrode potential, its value given as $\Delta G_u = eU$, e is the numbers of the electron transfer and U denotes the electrode potential. $\Delta G_{pH} = -k_B T \ln[H^+] = 2.303 K_B T * pH$, where B is Boltzmann constant and T is the temperature of the system. At standard condition (pH=0, T=298.15K) Gibb's energy of each intermediate was calculated as described below:

$$\Delta G_1 = \Delta E_{OH^*}$$

$$\Delta G_2 = \Delta E_{O^*} - \Delta E_{OH^*}$$

$$\Delta G_3 = \Delta E_{OOH^*} - \Delta E_{O^*}$$

$$\Delta G_4 = 4.92 - (\Delta G_1 + \Delta G_2 + \Delta G_3)$$

The mechanism of HER in alkaline medium involves the two-electron process:

$$M + H_2O \rightarrow M - H^* + OH^-$$

$$M - H^* + H_2O \rightarrow M^* + H_2 + OH^-$$

The adsorption energy was calculated using the equation:

$$\Delta E_{H^*} = E_{H^*} - E^* - \frac{1}{2}E_{H_2}$$

The Gibb's free energy of HER is given as

$$\Delta G_{H^*} = \Delta E_{H^*} - T\Delta S + \Delta ZPE$$

ΔZPE -TΔS is taken as 0.24 for H-atom adsorption, so

$$\Delta G_{H^*} = \Delta E_{H^*} + 0.24$$

Table S4. Total energy and adsorption energy of different adsorbates on the surface of CuZn-BTC electrode.

Surface	Total Energy (eV)	Adsorption energy (eV)
CuZn-BTC	-272.742	-
Cu-OH*	-281.519	2.703
Cu-O*	-274.913	5.915
Cu-OOH*	-285.105	7.205
Zn-OH*	-282.062	2.160
Zn-O*	-274.957	5.871
Zn-OOH*	-287.314	4.996
H_2O	-14.8747541	-
H_2	-6.787373128	-

Table S5. Total energy and adsorption energy of different adsorbates on the surface of Cu-BTC electrode.

Surface	Total Energy (eV)	Adsorption energy (eV)
Cu-BTC	-274.246	-
Cu-OH*	-283.116	2.6
Cu-O*	-277.286	5.04
Cu-OOH*	-287.73	6.08

Table S6. Total energy and adsorption energy of different adsorbates on the surface of Zn-BTC electrode.

Surface	Total Energy (eV)	Adsorption energy (eV)
Zn-BTC	-269.426	-
Zn-OH*	-279.844	1.06
Zn-O*	-273.077	4.436
Zn-OOH*	-284.67	4.32

Table S7. Gibb's free energy values of Cu-BTC, Zn-BTC, and CuZn-BTC.

Surface		ΔG_1 (eV)	ΔG_2 (eV)	ΔG_3 (eV)	ΔG_4 (eV)
Cu*-BTC	At U=0	2.58	2.43	1.037	-1.16
	At U= 1.23	1.38	1.206	-0.1929	-2.39
Zn*-BTC	At U=0	1.06	3.37	-0.11	-0.59
	At U= 1.23	-0.1669	2.14	-1.34	0.63
Cu*Zn-BTC	At U=0	2.703	3.212	1.29	-2.28
	At U= 1.23	1.473	1.982	0.06	-3.5

Table S8. Gibb's free energy values of CuZn-BTC at different adsorption sites (Cu and Zn)

Surface		ΔG_1 (eV)	ΔG_2 (eV)	ΔG_3 (eV)	ΔG_4 (eV)
Cu*Zn-BTC	At U=0	2.703	3.212	1.29	-2.28
	At U= 1.23	1.473	1.982	0.06	-3.5
CuZn*-BTC	At U=0	2.160	3.711	-0.87	-0.07
	At U= 1.23	0.930	2.481	-2.1	-1.3

Table S9. Total energy, Adsorption and Gibb's free energy of hydrogen adsorption on the CuZn-BTC electrode surface at different adsorption sites.

Surface	Total Energy (eV)	Adsorption energy (eV)	Gibb's energy (eV)
Cu -H*	-275.682	0.453	0.693275
Zn -H*	-277.092	-0.956	-0.71664

9. References.

1. E. Enkhtuvshin, S. Yeo, H. Choi, K. M. Kim, B. S. An, S. Biswas, Y. Lee, A. K. Nayak, J. U. Jang and K. H. Na, Surface Reconstruction of Ni–Fe Layered Double Hydroxide Inducing Chloride Ion Blocking Materials for Outstanding Overall Seawater Splitting, *Advanced Functional Materials*, 2023, 2214069.
2. A. Joshi, A. Gaur, P. Sood and M. Singh, One-Pot Crystallization of 2D and 3D Cobalt-Based Metal–Organic Frameworks and Their High-Performance Electrocatalytic Oxygen Evolution, *Inorg. Chem.*, 2021, **60**, 12685-12690.
3. F. He, Y. Zhao, X. Yang, S. Zheng, B. Yang, Z. Li, Y. Kuang, Q. Zhang, L. Lei and M. Qiu, Metal–Organic Frameworks with Assembled Bifunctional Microreactor for Charge Modulation and Strain Generation toward Enhanced Oxygen Electrocatalysis, *ACS nano*, 2022.
4. L. Zhao, B. Dong, S. Li, L. Zhou, L. Lai, Z. Wang, S. Zhao, M. Han, K. Gao and M. Lu, Interdiffusion reaction-assisted hybridization of two-dimensional metal–organic frameworks and Ti3C2T x nanosheets for electrocatalytic oxygen evolution, *ACS nano*, 2017, **11**, 5800-5807.
5. X. Zheng, Y. Cao, D. Liu, M. Cai, J. Ding, X. Liu, J. Wang, W. Hu and C. Zhong, Bimetallic metal–organic-framework/reduced graphene oxide composites as bifunctional electrocatalysts for rechargeable Zn–air batteries, *ACS applied materials & interfaces*, 2019, **11**, 15662-15669.
6. K. Maity, K. Bhunia, D. Pradhan and K. Biradha, Co (II)-doped Cd-MOF as an efficient water oxidation catalyst: doubly interpenetrated boron nitride network with the encapsulation of free ligand containing pyridine moieties, *ACS applied materials & interfaces*, 2017, **9**, 37548-37553.
7. K. Rui, G. Zhao, Y. Chen, Y. Lin, Q. Zhou, J. Chen, J. Zhu, W. Sun, W. Huang and S. X. Dou, Hybrid 2D dual-metal–organic frameworks for enhanced water oxidation catalysis, *Advanced Functional Materials*, 2018, **28**, 1801554.
8. Z. Gao, Y. Lai, L. Gong, L. Zhang, S. Xi, J. Sun, L. Zhang and F. Luo, Robust Th-MOF-Supported Semirigid Single-Metal-Site Catalyst for an Efficient Acidic Oxygen Evolution Reaction, *ACS Catalysis*, 2022, **12**, 9101-9113.
9. X. Zhang, R. Lin, X. Meng, W. Li, F. Chen and J. Hou, Iron Phthalocyanine/Two-Dimensional Metal–Organic Framework Composite Nanosheets for Enhanced Alkaline Hydrogen Evolution, *Inorganic Chemistry*, 2021, **60**, 9987-9995.
10. Z. Xue, Y. Li, Y. Zhang, W. Geng, B. Jia, J. Tang, S. Bao, H. P. Wang, Y. Fan and Z. w. Wei, Modulating electronic structure of metal-organic framework for efficient electrocatalytic oxygen evolution, *Advanced Energy Materials*, 2018, **8**, 1801564.
11. S. Gutiérrez-Tarriño, J. L. Olloqui-Sariego, J. J. Calvente, M. Palomino, G. Minguez Espallargas, J. L. Jorda, F. Rey and P. Ona-Burgos, Cobalt metal–organic framework based on two dinuclear secondary building units for electrocatalytic oxygen evolution, *ACS applied materials & interfaces*, 2019, **11**, 46658-46665.
12. X. Zhao, P. Pachfule, S. Li, T. Langenhahn, M. Ye, C. Schlesiger, S. Praetz, J. Schmidt and A. Thomas, Macro/microporous covalent organic frameworks for efficient electrocatalysis, *Journal of the American Chemical Society*, 2019, **141**, 6623-6630.

13. T. Tian, L. Huang, L. Ai and J. Jiang, Surface anion-rich NiS 2 hollow microspheres derived from metal–organic frameworks as a robust electrocatalyst for the hydrogen evolution reaction, *Journal of Materials Chemistry A*, 2017, **5**, 20985-20992.
14. K. Chen, C. A. Downes, E. Schneider, J. D. Goodpaster and S. C. Marinescu, Improving and Understanding the Hydrogen Evolving Activity of a Cobalt Dithiolene Metal–Organic Framework, *ACS Applied Materials & Interfaces*, 2021, **13**, 16384-16395.
15. M. Gu, S.-C. Wang, C. Chen, D. Xiong and F.-Y. Yi, Iron-Based Metal–Organic Framework System as an Efficient Bifunctional Electrocatalyst for Oxygen Evolution and Hydrogen Evolution Reactions, *Inorganic Chemistry*, 2020, **59**, 6078-6086.
16. J. Song, C. Zhu, B. Z. Xu, S. Fu, M. H. Engelhard, R. Ye, D. Du, S. P. Beckman and Y. Lin, Bimetallic cobalt-based phosphide zeolitic imidazolate framework: CoPx phase-dependent electrical conductivity and hydrogen atom adsorption energy for efficient overall water splitting, *Advanced Energy Materials*, 2017, **7**, 1601555.
17. J.-S. Qin, D.-Y. Du, W. Guan, X.-J. Bo, Y.-F. Li, L.-P. Guo, Z.-M. Su, Y.-Y. Wang, Y.-Q. Lan and H.-C. Zhou, Ultrastable polymolybdate-based metal–organic frameworks as highly active electrocatalysts for hydrogen generation from water, *Journal of the American Chemical Society*, 2015, **137**, 7169-7177.
18. I. Hod, P. Deria, W. Bury, J. E. Mondloch, C.-W. Kung, M. So, M. D. Sampson, A. W. Peters, C. P. Kubiak and O. K. Farha, A porous proton-relaying metal-organic framework material that accelerates electrochemical hydrogen evolution, *Nature communications*, 2015, **6**, 1-9.
19. Y. Li, B. Huang, Y. Sun, M. Luo, Y. Yang, Y. Qin, L. Wang, C. Li, F. Lv and W. Zhang, Multimetal borides nanochains as efficient electrocatalysts for overall water splitting, *Small*, 2019, **15**, 1804212.
20. M. Ali, E. Pervaiz and O. Rabi, Enhancing the Overall Electrocatalytic Water-Splitting Efficiency of Mo2C Nanoparticles by Forming Hybrids with UiO-66 MOF, *ACS omega*, 2021, **6**, 34219-34228.
21. K. Ao, J. Dong, C. Fan, D. Wang, Y. Cai, D. Li, F. Huang and Q. Wei, Formation of yolk–shelled nickel–cobalt selenide dodecahedral nanocages from metal–organic frameworks for efficient hydrogen and oxygen evolution, *ACS Sustainable Chemistry & Engineering*, 2018, **6**, 10952-10959.
22. M. Fiaz, M. Athar, S. Rani, M. Najam-ul-Haq and M. A. Farid, One pot solvothermal synthesis of Co3O4@ UiO-66 and CuO@ UiO-66 for improved current density towards hydrogen evolution reaction, *Materials Chemistry and Physics*, 2020, **239**, 122320.
23. D. Senthil Raja, X. F. Chuah and S. Y. Lu, In situ grown bimetallic MOF-based composite as highly efficient bifunctional electrocatalyst for overall water splitting with ultrastability at high current densities, *Advanced Energy Materials*, 2018, **8**, 1801065.
24. M. Zhang, W. Xu, T. Li, H. Zhu and Y. Zheng, In situ growth of tetrametallic FeCoMnNi-MOF-74 on nickel foam as efficient bifunctional electrocatalysts for the evolution reaction of oxygen and hydrogen, *Inorganic Chemistry*, 2020, **59**, 15467-15477.

25. X. Li, Z. Niu, J. Jiang and L. Ai, Cobalt nanoparticles embedded in porous N-rich carbon as an efficient bifunctional electrocatalyst for water splitting, *Journal of Materials Chemistry A*, 2016, **4**, 3204-3209.
26. Q. Zha, M. Li, Z. Liu and Y. Ni, Hierarchical Co, Fe-MOF-74/Co/carbon cloth hybrid electrode: simple construction and enhanced catalytic performance in full water splitting, *ACS sustainable chemistry & engineering*, 2020, **8**, 12025-12035.
27. A. Goswami, D. Ghosh, D. Pradhan and K. Biradha, In Situ Grown Mn(II) MOF upon Nickel Foam Acts as a Robust Self-Supporting Bifunctional Electrode for Overall Water Splitting: A Bimetallic Synergistic Collaboration Strategy, *ACS Applied Materials & Interfaces*, 2022, **14**, 29722-29734.
28. S. S. Sankar, G. Keerthana, K. Manjula, J. H. Sharad and S. Kundu, Electrospun Fe-incorporated ZIF-67 nanofibers for effective electrocatalytic water splitting, *Inorganic Chemistry*, 2021, **60**, 4034-4046.
29. G. Kresse and J. Furthmüller, Efficiency of ab-initio total energy calculations for metals and semiconductors using a plane-wave basis set, *Computational materials science*, 1996, **6**, 15-50.
30. Z. Ahmed, Krishankant, R. Rai, R. Kumar, T. Maruyama, C. Bera and V. Bagchi, Unraveling a Graphene Exfoliation Technique Analogy in the Making of Ultrathin Nickel–Iron Oxyhydroxides@ Nickel Foam to Promote the OER, *ACS Applied Materials & Interfaces*, 2021, **13**, 55281-55291.